Anomalous reactive transport in porous media: Experiments and modeling

Yaniv Edery, Ishai Dror, Harvey Scher, and Brian Berkowitz
Department of Earth and Planetary Sciences, Weizmann Institute of Science, 76100 Rehovot, Israel
(Received 18 February 2015; published 18 May 2015)

We analyze dynamic behavior of chemically reactive species in a porous medium, subject to anomalous transport. In this context, we present transport experiments in a refraction-index-matched, three-dimensional, water-saturated porous medium. A pH indicator (Congo red) was used as either a conservative or a reactive tracer, depending on the tracer solution pH relative to that of the background solution. The porous medium consisted of an acrylic polymer material formed as spherical beads that have pH-buffering capacity. The magnitude of reaction during transport through the porous medium was related to the color change of the Congo red, via image analysis. Here, we focused on point injection of the tracer into a macroscopically uniform flow field containing water at a pH different from that of the injected tracer. The setup yielded measurements of the temporally evolving spatial (local-in-space) concentration field. Parallel experiments with the same tracer, but without reactions (no changes in pH), enabled identification of the transport itself to be anomalous (non-Fickian); this was quantified by a continuous time random walk (CTRW) formulation. A CTRW particle tracking model was then used to quantify the spatial and temporal migration of both the conservative and reactive tracer plumes. Model parameters related to the anomalous transport were determined from the conservative tracer experiments. An additional term accounting for chemical reaction was established solely from analysis of the reactant concentrations, and significantly, no other fitting parameters were required. The measurements and analysis emphasized the localized nature of reaction, caused by small-scale concentration fluctuations and preferential pathways. In addition, a threshold radius for pH-controlled reactive transport processes was defined under buffering conditions, which delineated the region in which reactions occurred rapidly.

DOI: 10.1103/PhysRevE.91.052130 PACS number(s): 05.40.Fb, 47.56.+r, 47.70.−n, 82.33.Ln

I. INTRODUCTION

The evolution and spread of chemically reactive species as they migrate in geological and other porous media has been studied extensively in the literature over the last two decades. However, there remains a strong need for detailed experiments that provide high-resolution data sets to test models, and for improved models that can account for the complex patterns of reactive transport.

Modeling, design of appropriate experiments, and determination of representative measurements must address the key role of fluctuations in governing state variables (e.g., concentrations, velocities) caused by medium heterogeneities [1–4]. For reactive transport, experiments indicate that chemical reactions are localized to pore-scale sites, with medium heterogeneity affecting the nature of reactions and transport of reactants; the high degree of variability in pore-scale mixing impacts the larger-scale reactive transport behavior. As a consequence, e.g., the actual amount of mixing between reactants—and hence the amount of product—may be less than would be otherwise predicted by continuum models, due to averaging the concentrations and the mixing zone [5–7].

An important class of reactive transport experiments involves pH-induced [8–10] and bimolecular reactions [5,6,11–15]. The latter are designed so that a resident solution containing reactant B is displaced by an inflowing solution containing reactant A, to form a reaction product C. Many of these studies [6,11–15] employ rectangular, transparent-walled flow cells with dimensions of 10–30 cm and thickness of 1–5 cm, and yield measurements of concentrations at specific points or over the visible planar (wall) surface. Some of the constructed domains consist of periodic arrays of inclusions, and/or have relatively high porosity values [11,15], and thus are not representative of natural geological porous media. A notable exception employed natural cryolite particles as the porous medium, having a refraction index close to that of water, to enable measurement of spatial concentrations in two-dimensional (2D) cross sections of a 3D flow cell [6].

Modeling attempts to account for nonuniform mixing and reaction of reactants in both space and time are generally unable to reproduce key dynamics measured in laboratory experiments such as those described above [6,16]. Broadly, two modeling approaches are employed—namely continuum and particle tracking (PT)—and different models are based also on either a Fickian or anomalous (non-Fickian) accounting of the underlying transport.

A basic challenge of the continuum approach is to upscale from the pore level (or small scale) in such a way as to retain the main effect of fluctuations in velocities and concentrations [7]. The continuum approach generally relies on the Fickian-based advection-dispersion-reaction equation (ADRE) framework. The ADRE reactant concentration can be written in the form

$$\frac{\partial c_i}{\partial t} + v\frac{\partial c_i}{\partial x} - \frac{\partial}{\partial x}\left(D\frac{\partial c_i}{\partial x}\right) = r(c_A, c_B), \qquad (1)$$

where $c_i = c_i(x,t)$ $(i = A,B)$ is the concentration, v and D are the velocity and dispersion coefficients, respectively, and $r(c_A,c_B)$ is the total rate of product creation via reaction and source. Essentially all of the above-mentioned laboratory-scale studies have been interpreted on the basis of analytical and numerical solutions of the ADRE. In most cases, however, these solutions were found to be inadequate in capturing the (available) full spatial and/or temporal concentration measurements [6,8]. This is usually attributed [6] to effects of pore-scale fluctuations that are not accounted for by the ADRE. Furthermore, examination of a pH-induced reaction in a flow cell filled with glass beads under heterogeneous and

homogeneous packing [9] showed that heterogeneity enhances transverse mixing and mixing-controlled reaction. Note also that conventional continuum models are known to break down in reactive transport scenarios involving fast kinetics, even without the occurrence of anomalous transport for the passive transport component [17].

Related theoretical studies have developed reactive transport equations for bimolecular reactions by upscaling pore-scale diffusion-reaction equations [18,19], and by invoking a phenomenological Langevin model combined with an advection-diffusion equation [20]. In parallel, pore-scale simulations have also been examined in the context of reactive transport, e.g., based on a lattice Boltzmann model [21] and pore-scale and pore-network models for carbonate precipitation/dissolution [22]; such models are based on pore-scale images from (micro-)CT scans of small rock samples, and can include transport determined by, e.g., a Navier-Stokes flow model [23]. These models can be applied to examine pore-scale details, and as a basis for larger-scale models with externally estimated parameters needed to match reactive transport measurements.

As an alternative to (continuum) ADRE models, particle tracking (PT) models based on random walk formulations can be employed; reactions can be accounted for by using probabilistic rules of particle interaction in a PT scheme [24–34]. In the context of PT modeling, it is particularly effective to employ the continuous time random walk (CTRW) framework, which effectively accounts for anomalous (both conservative and reactive) tracer transport behavior. [We note that various theoretical and numerical formulations (but untested against experimental measurements) have been proposed to account for a range of chemical reactions, coupled mostly with anomalous diffusion, (e.g., [35–39]), although some authors have proposed equations for anomalous transport with reaction (e.g., [40–42]).] The CTRW-PT approach allows consideration of a wide range of probability density functions (PDF's) that govern the spatial and temporal aspects of the particle motion [43]. Implementations of a CTRW-PT approach have been tested under different reactive transport conditions, and demonstrated to be accurate and insightful, matching experimental measurements [7,44–46]. The CTRW-PT was shown to be effective in reaction diffusion dynamics [47]. The CTRW-PT can account for the occurrence of small-scale concentration fluctuations and the overall reaction dynamics in scenarios involving bimolecular reactive transport and multispecies reactive transport with dissolution and precipitation.

In terms of transport experiments involving chemical reactions, many technical difficulties exist with laboratory setups. Whether employing 1D columns or 2D/3D flow cells, most measurements provide information on concentration and reactions only at the inlet and outlet boundaries. Spatial concentrations can be determined by direct sampling of the solution (which is prone to disturb the flow field), by use of *in situ* probes (e.g., electrical conductivity, which has limited accuracy and is not selective to specific ions), or by the use of visualization techniques enabled by colorimetric reactions. In all of these measurements, the relevant sample support volume represents an average over one or more pores.

In this study, our specific objective was to focus on pH-driven chemical reactions, which are ubiquitous in soils and aquifers [48,49]. In this context, we established visualization experiments to provide detailed measurements of evolving spatial concentration distributions of reacting species, during transport, as a fundamental input to quantification of reaction patterns and dynamics in natural porous media. The experimental system overcomes measurement limitations described above. The measurements were based on a colorimetric reaction in a 3D flow cell; image analysis was employed to trace the dynamic spatial concentrations (averaged through the depth of the flow cell to yield 2D concentrations), of each reactant and product. We used a unique porous medium material with a refraction index equal to that of water. We then implemented a CTRW approach to interpret the reactive transport process. To model the dynamics, basic transport parameters were estimated using conservative column (1D) and flow cell (3D) experiments, as inputs to the full CTRW-PT reactive transport model. Acid-base titrations were conducted to quantify the buffering effect of the porous material. This information was incorporated in the reactive transport simulations; no additional fitting parameters were required.

II. EXPERIMENTAL METHODS

A. Porous medium and experimental setup

We employed four different sets of experiments to isolate the governing mechanisms that control reactive transport, and to enable estimation of model parameters (e.g., velocity, dispersion, reaction terms). First, 1D column experiments with a conservative tracer were used to determine the basic nature of transport in the specific porous medium and to extract estimates for basic transport parameters. Second, conservative tracer experiments in a 3D flow cell were used to examine multidimensional plume migration and enable estimation of other transport parameters (specifically transverse dispersion and angular displacement). Third, pH-induced reactive transport experiments in the same 3D flow cell were conducted. Fourth, independently, batch experiments were performed to quantify changes in pH due to a buffering effect of the porous medium.

In all of the experiments, the porous medium was fully water saturated. The refraction-index-matched porous medium consisted of cross-linked, modified acrylic polymer beads (JRM Chemical), spherical in shape, with diameters distributed uniformly from 1–4 mm, and with internal porosity of ∼90%. The internal hydraulic conductivity of the beads was very low, and negligible relative to the experiment time scales. The interbead porosity (i.e., not including the bead internal porosity) of the packed 1D column and 3D flow cell was 0.30, determined by standard weight measurement before and after packing. The beads were essentially transparent in the background solution, which consisted of deionized water with 10 g/L of KNO_3. The background fluid in the experiment was equilibrated with the beads, so that the beads had no influence on the pH background solution or the injected conservative tracer solution. However, for the reactive transport experiments, the polymer beads proved to have a buffering effect on the pH of the injected solution; this is discussed below in detail (Sec. II B).

The tracer used in all of the experiments was a standard pH indicator, Congo red (60 mg/L). The difference between

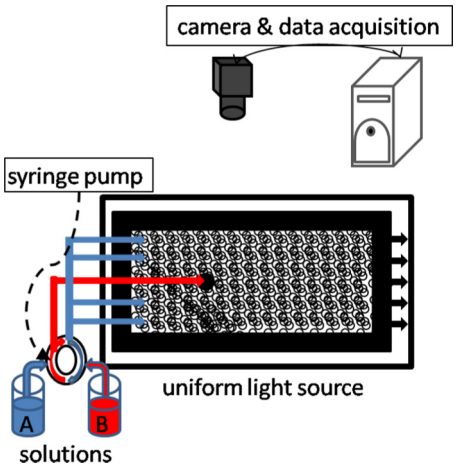

FIG. 1. (Color online) Schematic illustration of the experimental setup.

the conservative and reactive experiments lies in the pH of the injected Congo red solution, relative to the pH of the background solution. Congo red solution changes color from red at pH > 4 to blue at pH < 4. The pH of the background solution was 5.6, which is above the point of color change for Congo red. For the conservative tracer experiments, the pH of the injected Congo red solution was also 5.6, so that changes in color and intensity occurred only by dilution. For the reactive tracer experiments, the injected Congo red solution was pH $= 2.2$, with an initial blue color.

Batch experiments were performed to ensure that Congo red did not absorb to the beads at the pH levels used in the experiments. To avoid density effects, the Congo red was injected into the domain in a similar 10 g/L KNO_3 solution. Moreover, Congo red is a large molecule that does not enter the beads (confirmed experimentally). Thus, the Congo red advanced only in the pore space among the beads.

To first characterize the nature of transport in the porous medium (Fickian or anomalous), a cylindrical column (20 cm length and 2.7 cm internal diameter) was packed under saturated conditions with the acrylic polymer beads and tracer breakthrough curves were measured. The 1D column experiments were performed (in two replicates each) at three different flow rates, 0.5, 1, and 2 mL/min (Darcy fluid velocities of 0.29, 0.58, and 1.16 cm/min, respectively), which corresponded to the fluid velocities in the 3D flow cell experiments described below. In both column and flow cell experiments, a continuous step injection was employed; this was preferred to pulse injection because the buffering conditions (see below) led to a relatively fast rate of reaction for the reactive experiments. Outlet samples (1 mL) were obtained by a fraction collector (Foxy Jr. ISCO). Tracer concentrations were determined via calibration curves measured with a spectrophotometer (Cary 100).

Conservative and reactive tracer tests were then performed in a 3D flow cell with internal dimensions of 30 cm $\times$ 20 cm $\times$ 1.5 cm (see Fig. 1). The frame was made of PVC; the flow cell walls were extra clear glass (6 mm). A 4 mm diameter hole was drilled into the glass 10 cm from the inlet (x axis) and 10 cm from each of the two other boundaries (i.e., the upper and lower bound of the y axis). A septum sealed the hole and an hypodermic needle placed at a depth of $\sim$0.75 cm in the cell was used to inject the Congo red tracer (either as a conservative or a reactive experiment, depending on the pH of the injected solution).

The flow cell inlet consisted of four distributed holes (1.2 cm in diameter); five ports were placed along the outlet boundary. To control the flow, a twelve-channel high-precision pump (ISMATEC, IPC) was used both to introduce fluid at the inlet and to extract fluid from the outlet to ensure uniformity in flow. The flow cell was packed with the beads under saturated conditions. To verify uniformity of the flow field in the range of fluid velocities considered here, inert Congo red solution was injected in all four inlets; it was seen that the color distribution was uniform, with a defined front, at least $\sim$5 cm before reaching the injection port (i.e., at a distance of 5 cm from the inlet). To prevent bubble formation, the solution passed through air traps before reaching the inlets. Air traps also improved the uniformity of flow, dampening minor pulse flow effects created by the peristaltic pump. All experiments were performed at fixed room temperature. Inlet solution reservoirs were flushed with N_2 to remove dissolved gases (mainly CO_2). Conservative and reactive tracer experiments were conducted at three total volumetric flow rates of 2.5, 5, and 10 mL/min (divided equally among the inlet and injection ports), each in two replicates.

The flow cell was placed over a uniform light table (Kaiser Leuchtplatte, 5000 Kelvin color temperature) and photographed by a Nikon D90 camera that was controlled by Capture NX2 control software. Each picture was taken at prescribed time intervals and under the same conditions: uniform white balance, Iso - Lo1, focal length 50 mm, f/4.8, exposure time 1/80 sec, exposure bias +2.3. All pictures were extracted as raw data (nef files) and converted to 16 bit tiff files to achieve maximum resolution and quality. As illustrated in Fig. 1, the camera and flow cell were fixed at the same location and angle for all experiments to maintain reproducibility of the experiments. The room was kept dark (except for the light table) to prevent any light interference. An analysis of experiment component effects (light source, color dilution, camera effects, refraction index), in terms of magnitude and error, as described by Ref. [12], suggests that our experiment error within the measurements and image analysis is less than 5%. Details on the image processing are given in the Appendix.

B. Calculation of the pH buffering factor

The buffering capacity of the beads is a critical factor, because chemically, Congo red dissociates and releases protons as the pH rises, and vice versa; the stoichiometry of Congo red is shown in Fig. 2.

To quantify the buffering capacity of the beads, samples of solution containing beads were titrated gradually with diluted HCl solution at pH $= 2.1$ and the pH of the solution was recorded. In parallel a water sample was titrated to account for the dilution effects of the same HCl solution.

The buffering capacity of the beads, as compared to the water solution, was determined on the basis of the proton concentration in both solutions, at the same dilution factor. The

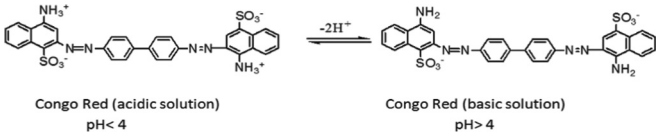

FIG. 2. Congo red stoichiometry. In aqueous solution, color is red at pH > 4, and blue at pH < 4.

buffering factor can be regarded as a retardation mechanism [50], in the sense that protons can be perceived to sorb onto the beads for given pH conditions and be released under different pH conditions. To estimate retardation [51], the initial proton concentration, the equilibrium proton concentration and the volume were calculated based on a bead mass of 0.53 g (in the sample tested), a solution volume of 9×10^{-3} L ($n = 0.30$ porosity for 30 mL sample), and a molar mass of 1 for the protons.

Based on the above, several sorption isotherm models were tested (linear, Langmuir, and Freundlich). The best fit was found for the Freundlich isotherm, as shown in Fig. 3. Considering a dry weight of the beads (2 g), per their volume (0.7×112 cm^3), we find the density of the beads to be $\rho_b = 25.4$mg/L.

Using the Freundlich slope ($K_d = 1.14$), we can calculate a retardation factor [51] using the definition $R_t = 1 + K_d\rho_b/n = 1.096$, with $R = K_d\rho_b/n = 0.096$. This formulation is used here as an approximation, recalling that the reaction is essentially instantaneous and irreversible for a given pH.

III. NUMERICAL MODELING FRAMEWORK

The CTRW-PT methodology for a conservative tracer, described in the Introduction and in detail in Sec.III A, was modified to simulate reactive transport by incorporating chemical reactions among Congo red "particles", according to their concentrations in a representative domain element. Both the conservative and the reactive tracer simulations followed the same conditions for advancing particles; the equations of motion are described in Sec. III A. Only the number of particle species under consideration differed: the conservative tracer required only one particle type, while three species (particle types) were introduced to account for reactive transport.

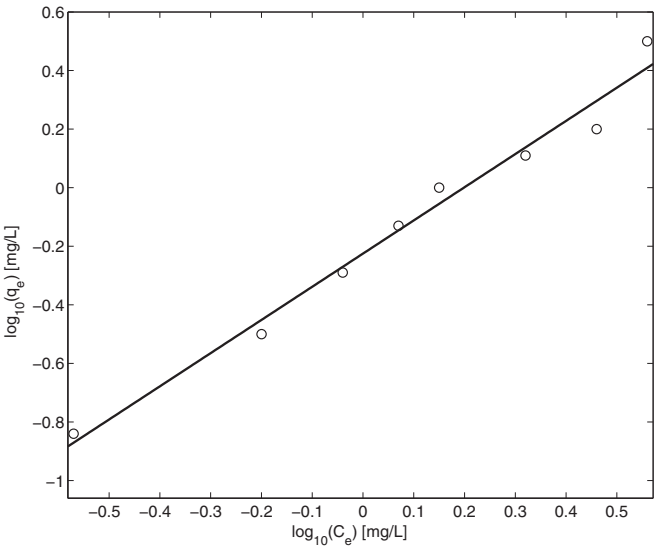

FIG. 3. C_e is the equilibrium concentration of the reactant and q_e is the sorbed concentration. Open circles are the sorption ratio between the $\log_{10}$ of the bulk to the $\log_{10}$ of the protons in mg/L. The line is the linear fit of the Freundlich sorption isotherm for protons in the beads containing solution. The slope of the fit is 1.14, which is the K_d of sorption by the Freundlich isotherm, $r^2 = 0.98$.

A. Continuous time random walk particle tracking (CTRW-PT)

The CTRW framework has been demonstrated to be highly effective in quantifying transport of conservative species in a wide range of homogeneous and heterogeneous porous media at various scales [52]. Anomalous (and as a special case, Fickian) transport can be described in terms of both partial differential equation and PT formulations [53]. The standard technique for the CTRW-PT model [43] is then modified to account for bimolecular reaction using an interaction radius of a pore scale [44,45], or multispecies reactions, which use grid elements to equilibrate competing reactive terms [46]. Recently, the interaction radius technique was shown [34] to have equivalent features to the colocation method [32]; the interaction radius is less computationally intensive.

In the CTRW-PT, the movement of each particle is governed by the equations of motion:

$$\mathbf{s}^{(N+1)} = \mathbf{s}^{(N)} + \boldsymbol{\varsigma}^{(N)}, \quad t^{(N+1)} = t^{(N)} + \tau^{(N)}, \tag{2}$$

where a random spatial increment $\boldsymbol{\varsigma}^{(N)}$ and a random temporal increment $\tau^{(N)}$ are assigned to each particle transition. For each N step, a velocity v can be derived by $\boldsymbol{\varsigma}^{(N)} / \tau^{(N)}$. It is emphasized that a wide range of space-time couplings and/or correlations can be accounted for with this simulation methodology, by appropriate definition of the increments $\boldsymbol{\varsigma}^{(N)}$ and $\tau^{(N)}$.

Here, a decoupled form of (2) is employed; the space-time particle transition PDF $\psi(\mathbf{s},t)$ can be written as

$$\psi(\mathbf{s},t) = F(\mathbf{s})\psi(t), \tag{3}$$

where $\boldsymbol{\varsigma}^{(N)}$ and $\tau^{(N)}$ are chosen from distinct and independent PDF's for space and time, $F(\mathbf{s})$ and $\psi(t)$, respectively.

When modeling with a two-dimensional polar coordinate system, accounting for the particle distribution in space requires introduction of an angle increment into the spatial part of the model, via a radius multiplication [43]. We therefore write (in two dimensions)

$$F(\mathbf{s})d\mathbf{s} = p(s)sds\Omega(\phi)d\phi. \tag{4}$$

The angle ϕ is distributed independently of $p(s)$ and $\psi(t)$, according to the $\Omega(\phi)$; it should be noted that in two dimensions, $p(s)$ has dimensions $1/L^2$.

In this formulation, the mean particle velocity, v_ψ, and the generalized particle dispersion, D_ψ, are defined as the first and second spatial moments of $p(s)/\bar{t}$, respectively [52]. Here $\bar{t}$ denotes the mean time (defined for $\beta > 1$) and $\overline{s_x}$ represents the mean step size in the x direction; in polar coordinates, this requires the factor $\cos(\phi)$ (note also the "volume" element

$sdsd\phi$). We thus write for v_ψ and D_ψ in the principal (x) direction of flow:

$$v_\psi = \frac{\overline{s_x}}{\overline{t}} = \frac{\int_0^\infty p(s)s^2 ds \int_{-\pi}^{\pi} \Omega(\phi)\cos(\phi)d\phi}{\int_0^\infty \psi(t)t dt}, \quad (5)$$

$$D_\psi = \frac{\overline{s_x^2}}{2\overline{t}} = \frac{\int_0^\infty p(s)s^3 ds \int_{-\pi}^{\pi} \Omega(\phi)\cos^2(\phi)d\phi}{2\int_0^\infty \psi(t)t dt}. \quad (6)$$

It is clear that the choice of PDF's $p(s)$, $\Omega(\phi)$, and $\psi(t)$ essentially determines the nature of the transport. For convenience, we focus here on an averaged, one-dimensional (uniform) flow domain, which is encountered in many laboratory experiments.

An advection-dispersion equation (ADE; Fickian) form of the PT simulations (ADE-PT) is considered first. Fickian transport is obtained from (2) and (3), and the angular distribution $\Omega(\phi)$ is included by defining

$$p(s) = \lambda_s^2 \exp(-\lambda_s s), \quad (7)$$

$$\psi(t) = \lambda_t \exp(-\lambda_t t), \quad (8)$$

$$\Omega(\phi) = \mathcal{N}(\phi, \sigma^2) \quad (9)$$

[with λ_s^2 the normalization factor for the two-dimensional $p(s)$]. The $\Omega(\phi)$ can be chosen from any distribution; we choose $\Omega(\phi)$ to be distributed normally with mean $\phi = 0$ and variance $\sigma = \pi/4$ due to its compactness. The distribution and associated parameters can depend on the experimental setup and flow/transport scenario of interest.

For the two-dimensional case, we use a normal distribution

$$\Omega(\phi) = \exp\left(-\phi^2/2\sigma_n^2\right)/\sigma_n\sqrt{2\pi}. \quad (10)$$

Inserting (10) into (5) yields

$$\int_{-\pi}^{\pi} \frac{\exp\left(-\phi^2/2\sigma_n^2\right)}{\sigma_n\sqrt{2\pi}} \cos(\phi)d\phi = \exp\left(-\sigma_n^2/2\right). \quad (11)$$

Solving the angular part for the second moment by inserting (10) into (6) yields

$$\int_{-\pi}^{\pi} \frac{\exp\left(-\phi^2/2\sigma_n^2\right)}{\sigma_n\sqrt{2\pi}} \cos(\phi)^2 d\phi = 1/2 + \exp\left(-2\sigma_n^2\right)/2. \quad (12)$$

A detailed accounting of the theoretical basis for this development is given elsewhere [43].

Inserting (7)–(9) into (5) and (6), while using (11) and (12) to account for the angular terms, which determine the velocity and dispersion components, yields

$$v_\psi = \frac{\exp(-\sigma^2/2)\int_0^\infty \lambda_s^2 \exp(-\lambda_s s)s^2 ds}{\int_0^\infty \lambda_t \exp(-\lambda_t t)t dt} \quad (13)$$

and

$$D_\psi = \frac{[1/2 + \exp(-2\sigma^2)/2]\int_0^\infty \lambda_s^2 \exp(-\lambda_s s)s^3 ds}{2\int_0^\infty \lambda_t \exp(-\lambda_t t)t dt}. \quad (14)$$

The values of λ_s and λ_t appearing in (7)–(9) are then determined from (13)–(14) by integrating the equations in time and space with a prescribed value of σ. The parameters λ_s and λ_t are unknown; they can be determined from the two resulting equations, for given v_ψ and D_ψ. It is clear that the values of these two coefficients will vary according to the prescribed mean velocity and generalized longitudinal dispersion. These PT parameters reproduce the ADE analytical expression:

$$\frac{\partial c_i}{\partial t} = \frac{\partial}{\partial x}\left(D\frac{\partial c_i}{\partial x}\right) - v\frac{\partial c_i}{\partial x}, \quad (15)$$

where the transport follows the Fickian assumption stating that the dispersion is constant in space and time.

To simulate anomalous transport conditions (CTRW-PT), the spatial distribution (7) and (9) for the ADE-PT is still employed. However, the temporal distribution is chosen to be the truncated power law (TPL) PDF [53]

$$\psi(t) = \mathcal{C}\frac{\exp(-t/t_2)}{(1 + t/t_1)^{1+\beta}}, \quad (16)$$

where $\mathcal{C}$ is a normalization coefficient. The TPL is governed by three parameters [52]: a power-law exponent β, a characteristic transition time t_1, and a cut-off time to Fickian transport t_2. The mean velocity and generalized longitudinal dispersion, v_ψ and D_ψ, are defined in (5)–(6) and (13)–(14), except that t_1 replaces $\overline{t}$ as a characteristic parameter. Thus $v_\psi = \overline{s_x}/t_1$ and $D_\psi = \overline{s_x^2}/2t_1$, and the denominators of (13) and (14) are replaced by t_1. The cut-off time parameter t_2 can be assigned a value according to the experimental conditions; larger values represent a range of time regimes over which transport behavior is anomalous. Inserting (7), (9), and (16) into (5) and (6), while using (11) and (12) to account for the angular terms, yields

$$v_\psi = \frac{\exp(-\sigma^2/2)\int_0^\infty \lambda_s^2 \exp(-\lambda_s s)s^2 ds}{t_1}, \quad (17)$$

and

$$D_\psi = \frac{[1/2 + \exp(-2\sigma^2)/2]\int_0^\infty \lambda_s^2 \exp(-\lambda_s s)s^3 ds}{2t_1}, \quad (18)$$

which is used to calculate the t_1 and λ_s. β, t_2, D_ψ, and σ are taken from the tracer tests (both column and flow cell) while v_ψ is calculated [53,54].

The model was developed in the C++ environment for efficiency, while using standard numerical recipes codes. During a simulation, particles are transported over a set of discrete observation intervals (i.e., time steps of fixed size). At each time step, the locations of all particles are recorded. By choosing a particle trajectory (distance vector and time required to traverse it), the velocity can be used to determine the location and fraction of time used to reach it at each simulation time step; the particle movement is recorded in midflight, and proceeds along the selected trajectory during the next simulation time step. As described below, this information is of particular value for proper quantification of reactive transport and accounting for tracer concentration in time [45]. A particular advantage of PT is its ability to account for small-scale (local) concentration fluctuations [46].

B. CTRW-PT with reactions: Simulation method

For the reactive transport case, various approaches could be considered to quantify the dynamics. We chose here a parsimonious formulation, defining three types of particles: A (inflowing particles denoting amount of Congo red, in moles), H (inflowing particles denoting H^+ quantity, in moles), and C

(quantity of reacted Congo red particles, in moles). Here, the range comprising the amount of injected H particles (pH 2.2 for the injected fluid) to zero [which is the relative background (resident) pH of 5.6] formed the pH scale. The local H values in each grid element established the local pH values, according to the pH scale.

Both A and H particles were injected into the system in the same location in the simulation; this mimicked the low pH (high proton concentration) of the injected Congo red solution.

Chemically, Congo red dissociates and release protons as the pH rises, and vice versa; the stoichiometry of Congo red is shown in Fig. 2. As noted above, the polymer beads were found to have a buffering effect on the solution pH, so that protons released by Congo red dissociation reacted with the beads (see Sec. II B). By considering capture and release of protons by the beads as a sorption (or "retardation") process, the buffering effect could be related to a Freundlich isotherm with a corresponding distribution coefficient (K_d), which was then incorporated in a "retardation factor".

The pH equation, $\mathrm{pH} = pK_a + \log_{10}(C_C/C_A)$, can be rewritten as follows:

$$[C] = \frac{[A]K_a}{[H^+]}, \tag{19}$$

where $[C]$ (Congo red after reaction, color red) and $[A]$ (Congo red prior to reaction, color blue) are the Congo red molar concentrations, while K_a is the threshold proton molar concentration for reaction and $[H^+]$ is the actual proton molar concentration. For these experimental conditions [55], $pK_a = 4$.

In our model, for each species, particle concentrations are expressed as a ratio between the species concentration in each grid element and the injected species concentration, and then compared to the experimental conditions:

$$\frac{R \cdot C_{H^+}}{N_{H^+}} = \frac{10^{-pH}}{10^{-2.2}} \tag{20}$$

$$\frac{C_A}{N_A} = \frac{[A]}{0.057 \times 10^{-3}} \tag{21}$$

$$\frac{C_C}{N_A} = \frac{[C]}{0.057 \times 10^{-3}}, \tag{22}$$

where C_A, C_C, and C_{H^+} are the concentrations of reactants in the model, per grid element, and R (retardation factor) is defined in Sec. II B. N_A and N_{H^+} are inflowing particle concentrations in the simulation; 0.057×10^{-3} and $10^{-2.2}$ are the inflowing molar concentrations of Congo red and protons in the experiments, respectively.

Inserting (20) into (19) and following some algebra, we obtain the following ratio:

$$\frac{C_C \cdot R \cdot C_{H^+} \times 10^{1.8}}{C_A \cdot N_{H^+}} = 1. \tag{23}$$

Hence, when the left side of Eq. (23) is smaller than one, the algorithm will dissociate simulated C_A to reach equilibrium. On the other hand, when the left side of Eq. (23) is greater than one, the algorithm will change the ratio by allowing reaction of simulated C_C to reach equilibrium.

Using an iterative process, values of A and C concentrations in each grid element were modified until the pH determined by this equation matched the pH value from the previously determined grid element H concentration (i.e., from the amount of H, modified by the retardation factor). Hence, the CTRW-PT simulations for reactive transport required no additional fitting parameters.

In the simulations, the molar ratio of injected A and H particles was maintained as in the experiment (0.057 mM Congo red and 6.3 mM protons). Therefore each particle in the simulation had a specific molar value, and a calculation of the molar values for the reactants was done iteratively for each grid element. At each time interval, $\Delta t = 6$ s, all particles in the system were frozen in midflight and the particle concentrations were determined. A MATLAB code was used to compare the molar values to the experiments. First, grid element A and C concentrations were transformed to a pH value according to $\mathrm{pH} = pK_a + \log_{10}(C_C/C_A)$. We then compared the simulated pH values to the experimental values.

IV. RESULTS AND DISCUSSION

A. Column experiments: Analysis and modeling

The 1D column tracer experiments were fit with a CTRW 1D solution (based on a partial differential equation formulation of the transport equation, equivalent to the 1D CTRW-PT formulation, as noted in Sec. III A), using the CTRW MATLAB toolbox [4,52]. Each experiment was conducted twice, and the breakthrough curves were fit with a CTRW solution using the truncated power law.

Figure 4 shows breakthrough curves corresponding to fluid velocities of $v = 1.16$, 0.29, and 0.58 cm/min; the error bars express the maximal difference between the two experiment repetitions. A semilog-in-time plot was employed to emphasize the long tailing of the tracer, characteristic of anomalous transport. For each experiment, the column was packed with new beads, which explain the variability between repetitions; while statistically homogeneous, each column packing represents a different porous medium realization. The main feature in this fit is the degree of the anomalous transport, expressed by $\beta = 1.74$ for all velocities. This indicates the level of heterogeneity in the medium [54]. As indicated in section 2, β, t_2, and longitudinal D can be fit by the CTRW to the breakthrough curve. The values of v and t_1 are calculated; v is calculated from the flow rate, domain dimensions, and porosity, while t_1 is extracted from Eqs. (17) and (18).

Figure 4 also shows the deviation of the ADE (Eq. 15) solution from the data and the deviation of the ADE-fitted velocity from the velocity calculated according to the inlet flux; the values reported are the optimal values fitted to the velocity (v) and dispersion (D) for the ADE. This further demonstrates the anomalous nature of the transport [54]. Anomalous transport and heterogeneity are related to preferential flow; these effects can be assessed mostly by the value of β. Note that in the CTRW model, β characterizes the nature of the dispersive transport, which is related to the domain heterogeneity; it was therefore held constant throughout the simulations here. A detailed study of the relationship and sensitivity among parameters in the CTRW framework can be found elsewhere [56].

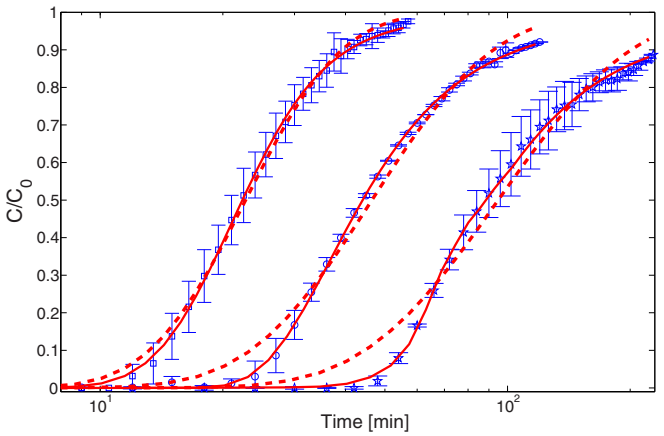

FIG. 4. (Color online) Column experiment breakthrough curves with CTRW (solid line) and ADE (dashed line) solution, for fluid flux (Q) of 2, 1, and 0.5 mL/min, which corresponds to velocities of 1.16, 0.58, and 0.29 cm/min (note the time is log scale, to emphasize the tailing behavior). Square symbols are for $Q = 2$ mL/min, ADE parameters (dashed line) are $v = 0.8$ cm/min and $D = 1.7$ cm^2/min, where the TPL fit (solid line) parameters are $v_\psi = 1.1$ cm/min, $D_\psi = 0.55$ cm^2/min, $\beta = 1.74$, $t_1 = 0.42$ min, and $t_2 = 10^{2.5}$ min. Circle symbols are for $Q = 1$ mL/min, ADE parameters (dashed line) are $v = 0.37$ cm/min and $D = 1.44$ cm^2/min where the TPL fit (solid line) parameters are $v_\psi = 0.55$ cm/min, $D_\psi = 0.068$ cm^2/min, $\beta = 1.74$, $t_1 = 2.2$ min, and $t_2 = 10^{3.4}$ min. Star symbols are for $Q = 0.5$ mL/min, ADE parameters (dashed line) are $v = 0.18$ cm/min and $D = 0.88$ cm^2/min where the TPL fit (solid line) parameters are $v_\psi = 0.27$ cm/min, $D_\psi = 0.098$ cm^2/min, $\beta = 1.74$, $t_1 = 4.8$ min, and $t_2 = 10^{5.7}$ min.

B. Flow cell tracer experiments

Conservative tracer experiments in the 3D flow cell were used to examine multidimensional plume migration, to ensure consistency with the above parameters estimated from the 1D column experiments, and to reevaluate dispersion (here with a transverse component) and angular displacement (which were not relevant in the 1D column). The value of D, based on the 1D column value, and the variance of the angle σ, were fitted by simulations from the CTRW-PT model [45,46,53]. The flow cell tracer experiments where simulated by CTRW-PT (see Sec. III A), where β and t_2 were used from the column experiment, v_ψ and t_1 were calculated, D_ψ was fitted based on the column value while accounting for the transverse component, which was not apparent in the 1D column flow (here, $D = 2 \times D_{longitudinal}$). The angle variance value σ, which can be regarded as width of the tortuosity distribution, was fitted by the CTRW-PT model as there was no prior information available. After each simulated 1 minute, a file of simulated Congo red particle concentrations per 1 cm $\times$ 1 cm was extracted.

To compare model simulations to experiments (both conservative and reactive), the simulated domain matched that of the flow cell experiment (30 cm $\times$ 20 cm with grid elements of 0.1 cm $\times$ 0.1 cm) in two dimensions; the depth was averaged by the image analysis to yield 2D concentration maps. The simulation results were then averaged spatially to a resolution of 1 cm $\times$ 1 cm, for comparison to the experiments. For the experiments, areas of 100 $\times$ 100 pixels were smoothed with a moving mean of 13 pixels, to reduce the image size to 300 $\times$ 200 grid elements of size 0.1 cm $\times$ 0.1 cm.

The tracer quantification in time and space can be seen in Figs. 5(a)–5(c), which is an image analysis transformation employing Fig. 8 (see Appendix) at three different times. Figures 5(d)–5(f) show the concentration of simulated tracer in space, the correspondence between the experiment and simulation is very good.

Figures 5(g)–5(i) show the local difference, for each grid element, between the transformed tracer experiment snapshot and the PT model. The correspondence between them is very good, though deviations occur on small scales. This can be expected because anomalous transport (low β) suggests the existence of preferential flow [54]. Preferential flows can be seen as distinct fingers of concentration difference along the y axis and are clearer in the forward propagation of the tracer. Reproducing these specific preferential flow paths cannot be done by an ensemble approach, such as the CTRW (or ADRE), because small-scale conductivity variations will lead to different flow patterns. Even so, the similarity between the experiment and the PT simulation is excellent; the two-sample Kolmogorov-Smirnov test in MATLAB [57,58], only in the region of the tracer zone, shows correspondence higher than 0.99 for all times. This test shows that the experiment and the model exhibit similar distribution functions, and therefore display the same underlying physics.

C. Flow cell reactive transport experiments

As noted in Sec. II, the injected Congo red solution was kept at pH = 2.2, while the background fluid was pH = 5.6. Due to the experiment configuration and the buffering effect of the beads, the injected pH changed rapidly to the background pH; reaction was rapid and relatively localized near the inlet, with relatively little mixing. Note that the protons could (over long time scales) move through the highly porous beads (i.e., there were no steric limitations) during the buffering process, but that the Congo red could not. Past the main region of reaction, the reaction product (red-colored Congo red at this higher pH) was only diluted subsequently; reverse reaction was improbable.

To simulate the reactive transport experiments with the CTRW-PT model, the same transport parameter values determined for the conservative transport experiments were employed (see also Sec. IV B). Due to the computational intensity of the PT simulation, a coarser grid (1 cm $\times$ 1 cm; as described above) was used to obtain results, requiring calculation times of days versus weeks.

At specific times, grid element comparisons were conducted between the experiment pH values, as extracted by image analysis, and pH values as extracted from the PT simulation. This is illustrated in Figs. 6(a)–6(c) (copper color range), which show the experiment pH values in a grid of 0.1 cm $\times$ 0.1 cm at times 4, 15, and 25 minutes, respectively. Figures 6(d)–6(f) (copper color range) show the results of the PT simulations. Visual comparison between simulation and experiment shows reasonable correspondence, especially given that no fitting parameters are employed in this complex system. Quantifying with the two-sample

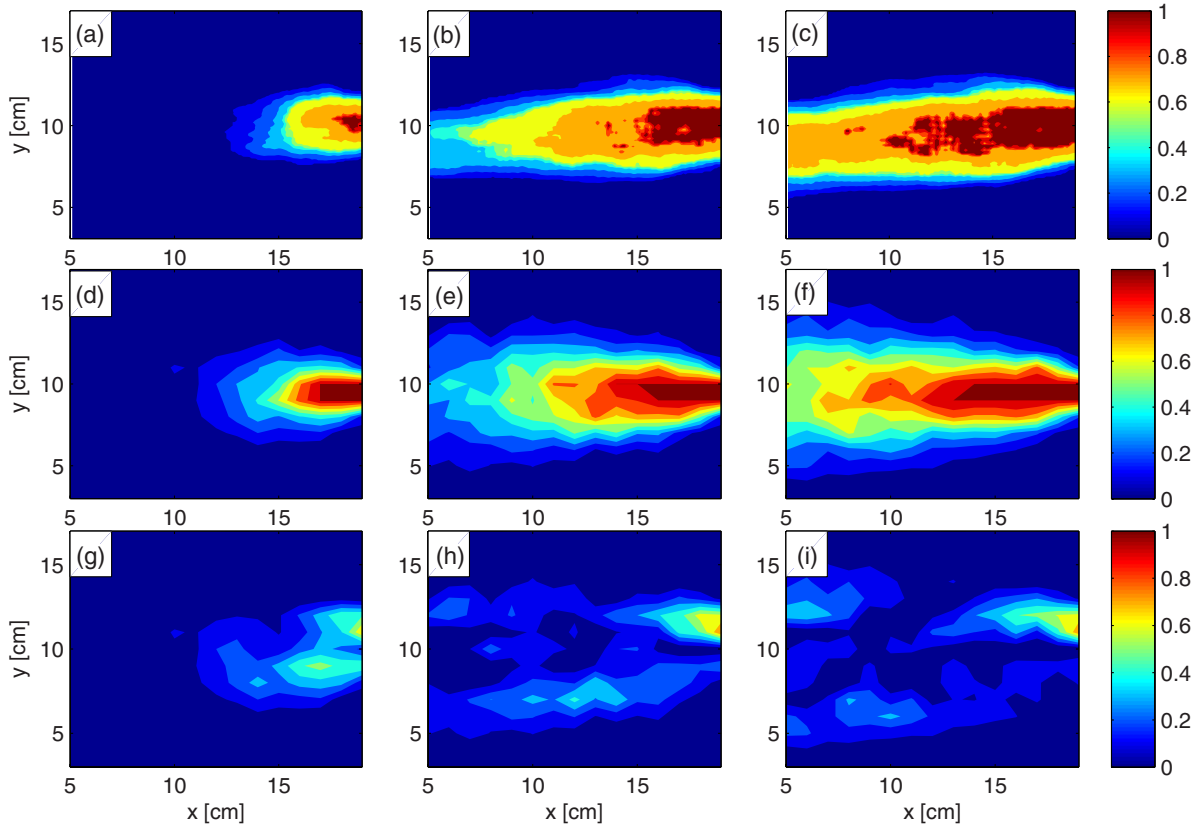

FIG. 5. (Color online) (a)–(c) Transformed Congo red tracer to concentrations of C/C_0 values in space at 4, 15, and 25 min, respectively; (d)–(f) C/C_0 spatial values of the PT simulation at 4, 15, and 25 minutes respectively; (g)–(i) Local difference (grid element to corresponding grid element) between tracer experiment and tracer PT simulation. In all figures, fluid flux was 10 mL/min, corresponding to a velocity of 1.16 cm/min (fluid velocities of 0.58 and 0.29 cm/min (fluxes 5 and 0.5 mL/min) were also studied but not shown).

Kolmogorov-Smirnov test in MATLAB [57,58], only in the reaction zone, the similarity was higher than 0.85 for all times. These simulations can be regarded as predictions in time and space, given that there was no change in parameter values over different times.

Further comparison between experiment and simulation of the pH values [between the copper color ranges shown in Figs. 6(a)–6(c) and 6(d)–6(f)] for each grid element can be seen in Figs. 6(g)–6(i) (shown here in a red-blue range in the same region). For this comparison to the CTRW-PT simulations, the experiment measurement domain was averaged to yield elements with resolution 1 cm × 1 cm. We emphasize that we did not aim for the simulation to reproduce exactly the same shape and pattern of the experiment, due to the effect of preferential flow (discussed below) and natural variation in experiments. Rather, comparison between experiment and simulation in Fig. 6 focused on the mean (ensemble) behavior in the reactive transport process, as a function of anomalous transport. As time progressed, a steady-state pH distribution was reached (pH values increase slowly without passing the pH = 4 threshold) and the concentration pattern that evolved toward the outlet was controlled only by dilution. The dilution pattern is shown in Figs. 6(a)–6(c) (red-blue color range), together with the model simulations (described in Sec. III B) in Figs. 6(d)–6(f) (red-blue color range). The agreement between them, in terms of the local difference (for each grid element) between the transformed tracer experiment snapshot and the PT model (normalized for the pH values), can be seen in Figs. 6(g)–6(i) (shown by the red-blue range in the same region). Moreover, the two-sample Kolmogorov-Smirnov test value for the dilution pattern was higher than 0.99 for all times.

The lack of fitting parameters in the CTRW-PT simulation, while maintaining a reasonable match to the reactive experiment, shows that the physical nature of flow (medium heterogeneity, transport, dispersion) and chemistry (pK_a, buffering effect) were well determined in the conservative tracer column and flow cell experiments, together with the batch tests. This experimental setup is novel in dissociating the physical and chemical aspects of reactive transport and attributing each parameter to the corresponding physical mechanism. The bead buffering capacity enabled observation of the ubiquitous effect of pH buffering in soil and the effect it has on reaction dynamics during transport.

The CTRW-PT simulations can quantify the transport and reaction on average, but cannot reproduce specific locations of preferential paths and reaction streaks. Any packing of the same porous material will yield different flow patterns, which are not reproducible and cannot be predicted a priori. The CTRW-PT mimicked the overall reaction behavior because it allowed for the correct tailing and the reaction pattern that follows.

Our experiments employed spherical beads with diameter of 1–4 mm; under these conditions, with the given velocities

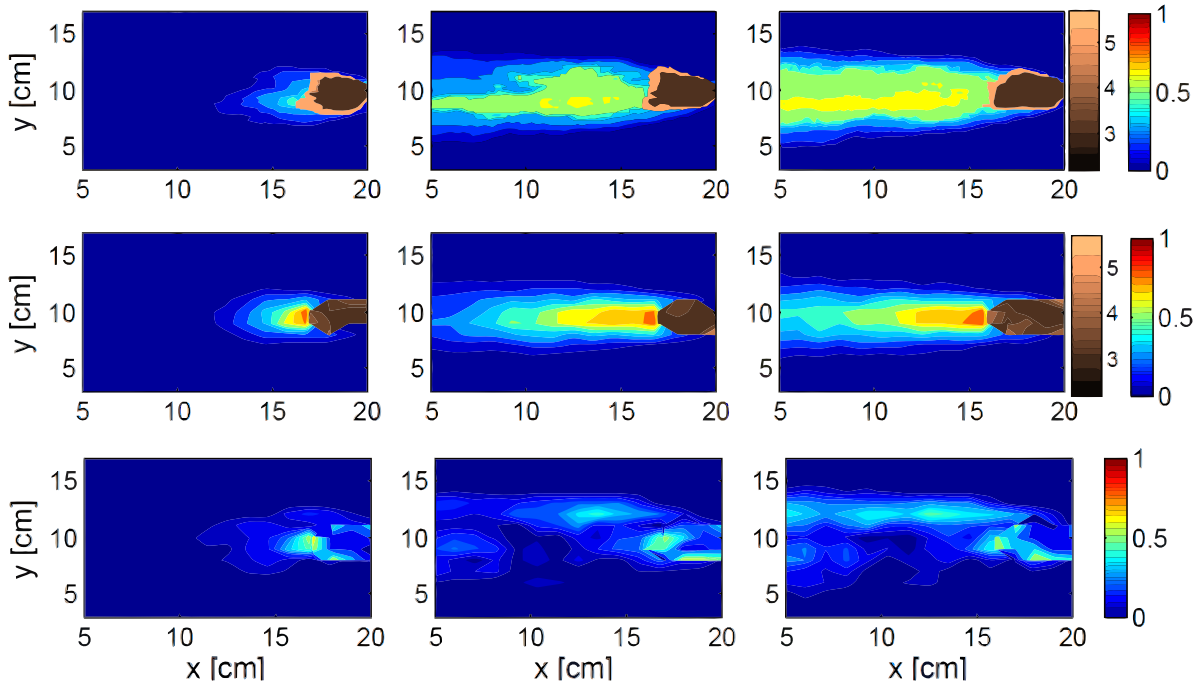

FIG. 6. (Color online) (a)–(c) Measurements of transformed Congo red reactive product to pH values in space (copper color range) and transformed Congo red dilution concentrations in spatial C/C_0 values (red to blue color range), at 4, 15, and 25 minutes, respectively (note that flow is right to left). (d)–(f) CTRW-PT simulations transformed to pH values (copper color range) and C/C_0 spatial values of the reactive PT simulation (red to blue color range) at 4, 15, and 25 minutes, respectively. (g)–(i) Local difference (grid element to corresponding grid element) between reactive experiment (pH and dilution) and reactive CTRW-PT simulation (pH and dilution). In all figures, fluid flux was 10 mL/min, corresponding to a velocity of 1.16 cm/min (fluid velocities of 0.58 and 0.29 cm/min (fluxes 5 and 0.5 mL/min) were also studied but not shown).

and domain size, the appearance of preferential (nonuniform) flow might not be expected. The role and importance of preferential flow in porous media has been studied extensively in the literature, e.g., [59–62]. Recently, a clear quantitative connection between preferential flow and the CTRW framework [54] showed that when preferential flow is more dominant, transport becomes more anomalous. In this context, it is clear that small-scale preferential flow was present in our system due to small-scale structure variation; the β value characterized the anomalous transport.

Indeed, qualitatively, preferential flow is clearly visible in Fig. 7(a); this is even more apparent in the transformation of pH values in Fig. 7(b). Careful examination of Figs. 7(a)–7(c) showed not only the existence of preferential flow (marked by an ellipse for convenience), but its persistence in both reacted and diluted Congo red. This flow pattern was stable over time, especially in the steady-state conditions of the reaction pattern; this can be seen in Fig. 7(c), where the origin of this specific flow path can be traced back to the reaction pattern in Fig. 7(b). The reaction was location-dependent due to these preferential flows and as such moving a few millimeters perpendicular to the flow would yield a significant change in the reaction rate values at steady state.

D. Threshold radius

While the reaction pattern in the experiments was heterogeneous, a plume of unreacted Congo red was established near the injection point. Because the buffering capacity of the beads is large, a local steady state was reached; the unreacted plume was governed by the intrinsic interplay between proton flux and buffering. Thus, the resulting unreacted plume can be delineated by a local-in-time reaction boundary, represented as a Fickian process. This plume size varied according to the flux. Approximating the unreacted plume with a circle (to assess the reaction front), as seen in Figs. 7(d)–7(f), yielded a threshold radius ($r_{\text{threshold}}$); within this radius, the pH threshold (of pH = 4, where the Congo red changes color around this pH value) was not reached and reaction was weak, while beyond it, the reaction is rapid and unreacted Congo red could only survive in the preferential flow paths. A standard ruler photographed with the flow cell during experiments was used to derive the ratio between pixel size and centimeters exactly from the Congo red concentration images.

Under the approximation of Fickian transport, the center of mass movement is identical to the fluid velocity (and therefore the focus is on a moving velocity frame), and the spreading extent of the plume is given by radial dispersion [63]. The Congo red reaction follows the pH (which is affected by the buffering effect of the beads) and to a lesser extent, on the Congo red concentration itself; hence, while the Congo red migration was confined to the pore space, its reaction pattern was strongly coupled to the pH change. Because the color change of the Congo red is due mainly to the pH threshold behavior, the focus of this analysis is on the protons and the concentration term (c) refers to the protons as proposed by Ref. [50]. The buffering capacity of the beads is large, so that the threshold radius varies slowly in time.

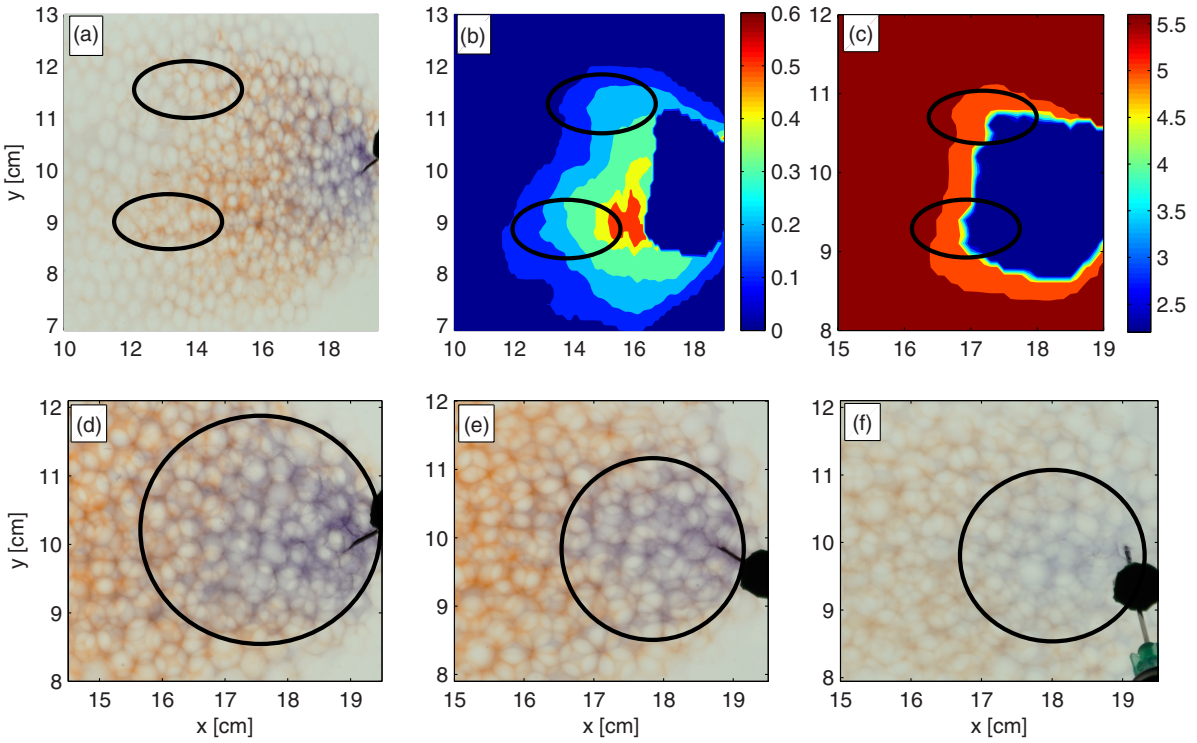

FIG. 7. (Color online) (a) Photo of the reactive transport experiment with flow rate of 10 mL/min [including 2 mL/min from the injection point (needle)]. A region of preferential flows is marked by an ellipse. (b) Transformation of the photo in (a) to Congo red dilution; the same preferential flows is marked by the ellipse. (c) Transformation of photo (a) to pH by Congo red color shift; the same preferential flow affecting the reaction is marked by an ellipse, and corresponds to the pH change. (d) Zoom in on the unreacted area of the 2 mL/min middle inlet; a circle with radius of 2.25 cm marks the unreacted Congo red. (e) Zoom in on the unreacted area of the 1 mL/min middle inlet; a circle with radius of 1.7 cm marks the unreacted Congo red. (d) Zoom in on the unreacted area of the 0.5 mL/min middle inlet; a circle with radius of 1.5 cm marks the unreacted Congo red.

Taking the radial form of the standard advection-dispersion equation [63,64] in one dimension coupled to a retardation factor (because of the measured buffer capability of the beads as described in Sec. II B), R_t, yields an ADRE in the form:

$$\frac{\partial c}{\partial t} + v\frac{\partial c}{\partial r} - \frac{\partial}{\partial r}\left(D\frac{\partial c}{\partial r}\right) = R_t\frac{\partial c}{\partial t}. \tag{24}$$

This is similar to the local equilibrium assumption (LEA) model as suggested by Ref. [65], but we focus on a nondimensional analysis and not on solving the equation [66] or the time moments. Here we replace v by the identity $v = Q/2\pi hnr$ for the radial direction, where n is porosity, Q is the injected volumetric flow rate, h is the depth of the flow cell, and r is the radius. Assuming that the advance in the direction of flow is a Galilean transformation and that for small times we have symmetry in the angular direction, we define $R_t = 1 + K_d\rho_b/n$ as given in Sec. II B.

We simplify Eq. (24) as follows:

$$\frac{\partial c}{D\partial t} = \frac{\Omega}{r}\frac{\partial c}{\partial r} + \frac{\partial c^2}{R\partial^2 r}, \tag{25}$$

where $\Omega = Q/2\pi hnDR$ and $R = K_d\rho_b/n$. We then perform a nondimensional analysis on Eq. (25) and write $D = \frac{\rho^2}{\tau}$ to replace r by $\xi = \frac{r}{\gamma}$. This results in the nondimensional equation

$$\frac{\partial c}{\partial t/\tau} = \frac{\Omega\rho^2}{\gamma^2}\frac{\partial c}{\xi\partial\xi} + \frac{\rho^2}{R\gamma^2}\frac{\partial c^2}{\partial^2\xi}, \tag{26}$$

where ρ is the characteristic length for dispersion and γ is the typical radius for equilibrium between the incoming flux to the dispersion and retardation. We are interested in the leading order of Eq. (26), specifically the equilibrium value of the first nondimensional moment:

$$\frac{\Omega\rho^2}{\gamma^2} = \frac{Q}{2\pi hnDR}\frac{\rho^2}{\gamma^2} = 1. \tag{27}$$

This can be transformed to a "threshold radius", $r_{\text{threshold}}$, defined as

$$r_{\text{threshold}} = \gamma = \rho\sqrt{\frac{Q}{2\pi hnDR}} \tag{28}$$

or, rather

$$r_{\text{threshold}} \propto \sqrt{\frac{Q}{2\pi hnDR}}, \tag{29}$$

which relates the extent of the unreacted plume to the flux, dispersion, and retardation values.

The approximated $r_{\text{threshold}}$ can be regarded as the local-in-time equilibrium radius for the proton density, which characterizes the spatial extent of the reaction plume (interplay mainly between buffering and flux, and to a lesser extent,

dispersion). In Eq. (29), there is a local equilibrium (per volume) between the incoming proton flux and the combined effect of dispersion and retardation. The latter effects decrease the proton density, and therefore change the pH. This can be related directly to the color transition seen in our experiments for all fluxes. Here, $n = 0.3$, $h = 1.5$ cm, R was calculated to be 0.096 (see Sec. II B), Q (single point of injection) had three flow rates 0.5, 1, and 2 mL/min that were related to three (Fickian) dispersion coefficients, 0.88, 1.44, and 1.7 cm^2/min, respectively. Using Eq. (29), we found $r_{threshold}$ to be 1.49, 1.65, and 2.15 cm for $Q = 0.5, 1$ and 2 mL/min, respectively; this corresponded directly to the measured radius [see Figs. 7(d)–7(f)] for the unreacted Congo red in our experiment: 1.5, 1.7, and 2.25 cm for the corresponding fluxes.

V. CONCLUDING REMARKS

The multistep approach presented here is crucial in decoupling the different mechanisms governing reactive transport phenomena. The transition between 1D and 2D tracer experiments enables quantification of the heterogeneity effects of the domain on transport. Independent batch experiments measured the buffering effect of the porous medium. Combining all of these parameters within the CTRW-PT model resulted in simulations that mimicked the reactive transport experiment measurements, without any model fitting parameters for the reactions. This approach was possible because the reaction was well defined and fast, and the buffering effect limited the size of the reaction plume. The ability to define a threshold radius demonstrated the limited extent of the principal region of reaction. We employed the modeling analysis to delineate the physical transport and reaction mechanisms, rather than to determine parameters that provide an exact fit to the measurements (e.g., β characterized the domain heterogeneity, and was held constant in all simulations).

While the reactive CTRW-PT used the transport parameters extracted from the conservative tracer experiments, it was the interaction between transport and reaction mechanisms in a statistical manner (PT model) that captured the tracer migration and reaction. As such, reaction followed the fluctuating nature of tracer advance rather than an average behavior. The modeling analysis and experimental methods presented here are generic and can be applied and adapted to other chemical reaction and porous medium scenarios.

ACKNOWLEDGMENTS

This research was supported by the Israel Water Authority (Grant No. 450056884).

APPENDIX: IMAGE PROCESSING

To establish the ratio between color intensity and tracer concentration, a calibration curve was determined. Known concentrations of Congo red were injected into a representative cell (with the same thickness as that of the 3D flow cell; Fig. 1) filled with beads and photographed under the same conditions described above. Image analysis was employed to calculate an average color intensity of RGB (red-green-blue); for each color, the calibration curve can be seen in Fig. 8(a). Because the

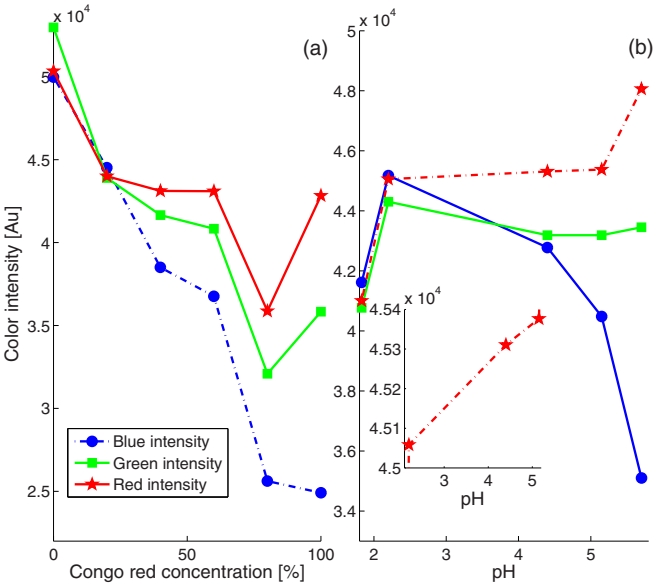

FIG. 8. (Color online) (a) Calibration curve for dilution of Congo red. (b) Calibration curve for pH vs RGB intensity; the inset shows the linear trend between the relevant pH transitions and the red intensity.

blue wavelength was monotonic with concentration, there was no need to use the other wavelengths to account for dilution-concentration effects. Linear interpolation was employed between consecutive points and used to translate average dilution intensity in the flow experiment to concentration.

A similar calibration curve was determined to analyze the reactive transport experiments, which involve variations in pH, to properly account for the colorimetric reaction and connect each color to a pH value. This was done, as described for the conservative tracer, by photographing a representative cell (same depth) filled with beads and with Congo red under varying pH values. The calibration curve is shown in Fig. 8(b); here the red wavelength intensity displays monotonicity (especially at the relevant pH range, as seen in the inset) and was used as the calibration wavelength between pH to intensity. The image analysis algorithm first used the initial picture without any Congo red as the initial state. Hence, if there was less than a 5% difference between the initial state and any following picture, it was not accounted for. This allowed us to ignore areas not penetrated by Congo red, thus increasing the efficiency of analysis. This 5% value is also the maximum difference between the mean value of color intensity and the local value of intensity given by the moving average method. The algorithm accounted for pH changes by the change in red intensity, which is less than 4.5×10^4 [see Fig. 8(b)]. The Congo red color after the reaction is red and can only dilute to white, as such the red intensity in the RGB scheme was always higher than 4.5×10^4. This allowed us to fix the pH value to 5.6, in accord with the red intensity throughout our experiment. For the remaining parts of the pictures, i.e., where reactions did not occur, we used the dilution curve to relate intensity to dilution.

A MATLAB program was developed for image processing of the photographs from the flow cell conservative and reactive tracer experiment. In each frame, the edge of the flow cell

was identified to prevent interference with the analysis. A moving mean was calculated in the relevant area of about 100 × 100 pixels (equivalent to 0.2 mm × 0.2 mm), to reach a corresponding RGB value for the calibration curve in Fig. 8. The moving mean jumped every 13 pixels to reduce the image size from 4000 × 3000 pixels to 300 × 200 concentration grid elements. The smaller number of grid elements simplified computational treatment, mainly because each experiment yielded hundreds of pictures with 10-second differences between frames.

The flow cell had three dimensions by nature and due to the point injection of Congo red. The Congo red was effectively averaged over depth by the image analysis to represent a 2D plume advance in an effective 1D flow field.

[1] M. Rashidi, L. Peurrung, A. F. B. Tompson, and T. J. Kulp, Adv. Water Resour. **3**, 163 (1996).
[2] J. Cao and P. K. Kitanidis, Water Resour. Res. **8**, 1941 (1998).
[3] R. Metzler, J. Klafter, and I. M. Sokolov, Phys. Rev. E **58**, 1621 (1998).
[4] A. Cortis, Y. Chen, H. Scher, and B. Berkowitz, Phys. Rev. E **70**, 041108 (2004).
[5] D. S. Raje and V. Kapoor, Environ. Sci. Technol. **34**, 1234 (2000).
[6] C. M. Gramling, C. F. Harvey, and L. C. Meigs, Environ. Sci. Technol. **36**, 2508 (2002).
[7] Y. Edery, A. Guadagnini, H. Scher, and B. Berkowitz, Adv. Water Resour. **51**, 86 (2013).
[8] S. C. Jose and O. A. Cirpka, Environ. Sci. Technol. **38**, 2089 (2004).
[9] M. Rolle, C. Eberhardt, G. Chiogna, A. O. Cirpka, and P. Grathwohl, J. Contam. Hydrol. **110**, 130 (2009).
[10] S. Loyaux-Lawniczak, F. Lehmann, and P. Ackerer, J. Contam. Hydrol. **138-139**, 15 (2012).
[11] T. W. Willingham, C. J. Werth, and A. J. Valocchi, Environ. Sci. Technol. **42**, 3185 (2008).
[12] M. Konz, P. Ackerer, E. Meier, P. Huggenberger, E. Zechner, and D. Gechter, Hydrol. Earth Sys. Sci. **12**, 727 (2008).
[13] M. Konz, P. Ackerer, A. Younes, P. Huggenberger, and E. Zechner, Water Resour. Res. **45**, 1944 (2009).
[14] E. Castro-Alcalá, D. Fernández-Garcia, J. Carrera, and D. Bolster, Environ. Sci. Technol. **46**, 3228 (2012).
[15] P. de Anna, J. Jimenez-Martinez, H. Tabuteau, R. Turuban, T. Le Borgne, M. Derrien, and Y. Méheust, Environ. Sci. Technol. **48**, 508 (2014).
[16] G. E. Katz, B. Berkowitz, A. Guadagnini, and M. W. Saaltink, J. Contam. Hydrol. **120-121**, 27 (2011).
[17] P. E. Kechagia, I. N. Tsimpanogiannis, Y. C. Yortsos, and P. C. Lichtner, Chem. Eng. Sci. **57**, 2565 (2002).
[18] G. M. Porta, J.-F. Thovert, M. Riva, A. Guadagnini, and P. M. Adler, Phys. Rev. E **86**, 036102 (2012).
[19] G. M. Porta, M. Riva, and A. Guadagnini, Adv. Water Resour. **35**, 151 (2012).
[20] A. M. Tartakovsky, Phys. Rev. E **82**, 026302 (2010).
[21] F. Jiang and T. Tsuji, Phys. Rev. E **90**, 053306 (2014).
[22] C. Varloteaux, M. T. Vu, S. Békri, and P. M. Adler, Phys. Rev. E **87**, 023010 (2013).
[23] B. Bijeljic, A. Raeini, P. Mostaghimi, and M. J. Blunt, Phys. Rev. E **87**, 013011 (2013).
[24] D. Gillespie, J. Comput. Phys. **22**, 403 (1976).
[25] R. Fabriol, J. P. Sauty, and G. Ouzounian, J. Contam. Hydrol. **13**, 117 (1993).
[26] N. Z. Sun, Water Resour. Res. **35**, 3649 (1999).
[27] Y. Cao, D. Gillespie, and L. Petzold, J. Comput. Phys. **206**, 395 (2005).
[28] J. Palanichamy, T. Becker, M. Spiller, J. Köngeter, and S. Mohan, Computing Visualization Sci. **12**, 51 (2009).
[29] G. Srinivasan, D. M. Tartakovsky, B. A. Robinson, and A. B. Aceves, Water Resour. Res. **43**, W12415 (2007).
[30] S. B. Yuste, J. Klafter, and K. Lindenberg, Phys. Rev. E **77**, 032101 (2008).
[31] S. B. Yuste, L. Acedo, and K. Lindenberg, Phys. Rev. E **69**, 036126 (2004).
[32] D. A. Benson and M. M. Meerschaert, Water Resour. Res. **44**, W12201 (2008).
[33] Y. Zhang and C. Papelis, Phys. Rev. E **84**, 066704 (2011).
[34] S. Hansen, B. Berkowitz, and H. Scher, Adv. Water Resour. **69**, W07524 (2014).
[35] I. M. Sokolov, M. G. W. Schmidt, and F. Sagués, Phys. Rev. E **73**, 031102 (2006).
[36] A. Yadav and W. Horsthemke, Phys. Rev. E **74**, 066118 (2006).
[37] D. Campos, S. Fedotov, and V. Méndez, Phys. Rev. E **77**, 061130 (2008).
[38] A. Zoia, Physical Review E **77**, 041115 (2008).
[39] D. Froemberg, H. H. Schmidt-Martens, I. M. Sokolov, and F. Sagués, Phys. Rev. E **83**, 031101 (2011).
[40] E. Abad, S. B. Yuste, and K. Lindenberg, Phys. Rev. E **81**, 031115 (2010).
[41] S. Fedotov, Phys. Rev. E **81**, 011117 (2010).
[42] C. N. Angstmann, I. C. Donnelly, and B. I. Henry, Phys. Rev. E **87**, 032804 (2013).
[43] M. Dentz, H. Scher, D. Holder, and B. Berkowitz, Phys. Rev. E **78**, 041110 (2008).
[44] Y. Edery, H. Scher, and B. Berkowitz, Geophys. Rev. Lett. **36**, L02407 (2009).
[45] Y. Edery, H. Scher, and B. Berkowitz, Water Resour. Res. **46**, W07524 (2010).
[46] Y. Edery, H. Scher, and B. Berkowitz, Water Resour. Res. **47**, W08535 (2011).
[47] Y. Berkowitz, Y. Edery, H. Scher, and B. Berkowitz, Phys. Rev. E **87**, 032812 (2013).
[48] G. Sposito, *The Chemistry of Soils* (Oxford University Press, Oxford, 1989).
[49] R. P. Schwarzenbach, P. M. Gschwend, and D. I. Imboden, Environmental Organic Chemistry, 2nd ed. (Wiley, New York, 2003).
[50] A. Scheidegger, C. S. Bürgisser, M. Borkovec, H. Sticher, H. Meeussen, and W. van Riemsdijk, Water Resour. Res. **30**, 2937 (1994).
[51] R. A. Freeze and J. A. Cherry, *Groundwater* (Prentice Hall, Upper Saddle River, New Jersey, 1979).

[52] B. Berkowitz, A. Cortis, M. Dentz, and H. Scher, Rev. Geophys. **44**, RG2003 (2006).
[53] M. Dentz, A. Cortis, H. Scher, and B. Berkowitz, Adv. Water Resour. **27**, 155 (2004).
[54] Y. Edery, A. Guadagnini, H. Scher, and B. Berkowitz, Water Resour. Res. **50**, 1490 (2014).
[55] Z. L. Yaneva and N. V. Georgieva, Inter. Rev. Chem. Eng. **4**, 127 (2012).
[56] V. Ciriello, A. Guadagnini, V. D. Federico, Y. Edery, and B. Berkowitz, Water Resour. Res. **49**, 5206 (2013).
[57] F. J. J. Massey, J. Am. Stat/ Assoc. **46**, 68 (1951).
[58] G. Marsaglia, W. W. Tsang, and J. Wang, J. Stat. Software **8**, 1 (2003).
[59] M. Bianchi, C. Zheng, C. Wilson, G. R. Tick, G. Liu, and S. M. Gorelick, Water Resour. Res. **47**, W05524 (2011).
[60] A. Fiori and I. Jankovic, Math. Geosci. **44**, 133 (2012).
[61] M. Riva, A. Guadagnini, D. Fernandez-Garcia, X. Sanchez-Vila, and T. Ptak, J. Contam. Hydrol. **101**, 1 (2008).
[62] M. Riva, L. Guadagnini, and A. Guadagnini, Stoch. Environ. Res. Risk Assess. **24**, 955 (2010).
[63] P. A. Hsieh, Water Resour. Res. **22**, 1597 (1986).
[64] J. A. Hoopes and D. R. F. Harleman, J. Geophys. Res. **72**, 3595 (1967).
[65] A. J. Valocchi, Water Resour. Res. **22**, 1693 (1986).
[66] A. F. Moench, Water Resour. Res. **25**, 439 (1989).